Nonlinear Dyn (2023) 111:97–112
https://doi.org/10.1007/s11071-022-07860-2

ORIGINAL PAPER

Band degeneration and evolution in nonlinear triatomic metamaterials

Chen Gong · Xin Fang · Li Cheng

Received: 29 May 2022 / Accepted: 26 August 2022 / Published online: 30 September 2022

Abstract Nonlinear metamaterials exhibit unique features allowing for wave manipulation. Despite the increasing attention received, the underlying physical mechanisms and the evolution process of the band structures and bandgaps in strongly nonlinear metamaterials remain unclear. Here we establish and examine four strongly nonlinear metamaterial models (triatomic models) to show the evolution process of typical nonlinear band structures using analytical and numerical approaches. We find that the strongly nonlinear triatomic models present particular band degeneration and bifurcation, accompanied with the wave mode transfer in their unit cells. The evolution processes and the physical mechanisms of the band degeneration in different models are clarified with the consideration of the mode transfer. The observed degeneration exhibits shifting, bifurcating, shortening, merging or disappearing of dispersion curves, all depending on the arrangement of the coupled nonlinear elements. Meanwhile, the dimension of the unit cell reduces, alongside changes in the frequency range and mechanisms (Bragg and local resonance) of the bandgaps. These findings provide answers to some essential questions pertinent to the study of nonlinear periodic structures, nonlinear crystals and nonlinear metamaterials, which are of interest to the broad community of nonlinear physics.

Keywords Strongly nonlinear metamaterials · Band degeneration · Wave mode transfer · Coupled nonlinear elements

C. Gong · X. Fang (✉) · L. Cheng (✉)
Department of Mechanical Engineering, Hong Kong Polytechnic University, Hung Hom, Kowloon 999077, Hong Kong
e-mail: xinfangdr@sina.com

L. Cheng
e-mail: li.cheng@polyu.edu.hk

X. Fang
Laboratory of Science and Technology On Integrated Logistics Support, College of Intelligent Science and Technology, National University of Defense Technology, Changsha 410073, Hunan, China

1 Introduction

Band structures are essential features of periodic structures including conventional crystals and more advanced superlattices [1–3]. Metamaterials are superlattice structures featuring exceptional subwavelength functionalities which are unusual to nature materials such as perfect absorption, negative refraction, asymmetric transmission and phase modulation [4–10]. Despite the extensive attention received, most studies on superlattices and metamaterials are limited to linear systems. Based on Bloch theorem, band structures of various types of linear metamaterials are well understood and tactically structured to achieve

nonclassical wave functionalities exemplified by topological insulators. Bandgaps can also entail efficient suppression of elastic wave and vibrations, a salient feature that can be obtained through manipulating bandgaps and the subsequent wave propagation by tuning material and structural parameters.

Nonlinear metamaterials can enable properties/behaviors that are inaccessible and potentially superior to their linear counterparts, such as harmonic generation [11, 12], phase matching [13, 14], nonlinear resonance shifting [15–18], dispersion modulation [19–21], chaos [11, 22, 23], breathers [24–26] and solitons [27–29]. Recently, strongly nonlinear elastic/acoustic metamaterials (NAMs), consisting of periodic nonlinear local resonators, were shown to offer ultralow and ultra-broadband vibration suppression arising from the chaotic band effects [30] and the bridging coupling of bandgaps [23] among other salient features specific to nonlinear metamaterials. The Bragg and locally resonant bandgaps in a NAM are amplitude-dependent [15, 19–23, 30–42]. This property has been extensively investigated using the perturbation method [19, 35–37, 41], harmonic balance method [15, 20], homotopy analysis method [22, 38] and equivalent method [23, 33, 39, 43, 44]. With increasing wave amplitude, bandgaps in a NAM show complex variation such as shifting [15, 19–23, 31, 33–37, 41, 42], switching and eventually mutual coupling among them [32, 38–40]. In a weakly nonlinear diatomic granular chain, it was observed that a propagative band can transit to a bandgap due to the amplitude-dependent effects [32]. In a strongly nonlinear triatomic chain, bandgap effect can be adaptively broadened along with the wave amplitude attenuation during propagation, which leads to broadband acoustic limiting [39]. Wave transmission within nonlinear bandgaps also features multiple stability behavior. Excessive nonlinearity may even lead to the disappearance of some bandgaps [38, 39]. Recently, the spectro-spatial properties of wave propagation in a weakly nonlinear metamaterial consisting of nonlinear chain with multiple nonlinear local resonators are investigated by using perturbation method and 2D Fourier transform [36]. However, the perturbation results [36] failed to predict the behavior of the nonlinear system in regions near the frequency of pseudo-bandgaps (i.e., the shifted bandgap by amplitude).

Therefore, although the amplitude-dependent bandgaps in nonlinear metamaterials have attracted broad attention, the rich phenomena incurred, especially in strong nonlinear models, have not been well understood. Particularly, the underlying physical mechanisms and the evolution process of these peculiar bandgap phenomena remain largely unclear. For example, as a result of the bandgap shifting under strongly nonlinearity, the band structure reflected by the dispersion curves changes; but the underpinning reasons, the associated evolution process as well as its influences on the wave propagation remains unknown. This is seen as one of the bottlenecking problems which hinder the exploration of the NAM-specific properties as well as the applications of strongly nonlinear metamaterials.

In this paper, we establish four one-dimensional metamaterials models to elucidate the evolution process of typical nonlinear band structures and explore the underlying physical mechanisms. In Sect. 2, we introduce the models alongside the analytical method for band structure analysis. In Sect. 3, we take a typical case to demonstrate our methods. In Sect. 4, based on a typical model, we report and scrutinize the band degeneration and merging phenomenon and analyze the evolution of the band structure and the associated wave modes. In addition, we explore the adaptive broadening bandgap effect and validate the applicability of Bloch theorem. In Sect. 5, we first consider two other models to show the generality of the band degeneration phenomenon. In addition to the discovery of other types of band degeneration, we consider one more model along with the above three models to show the property of dimensionality reduction and establish the common features in these four nonlinear models and their relationships.

2 Metamaterials model and analysis methods

A nonlinear triatomic chain with two local resonators offers two nonlinear resonant bandgaps and a Bragg bandgap that may shift, merge, switch and couple. Therefore, a triatomic chain is a versatile metamaterial model that can showcase typical wave dynamics in nonlinear metamaterials. Here, we establish an infinite model to investigate the dispersion properties and

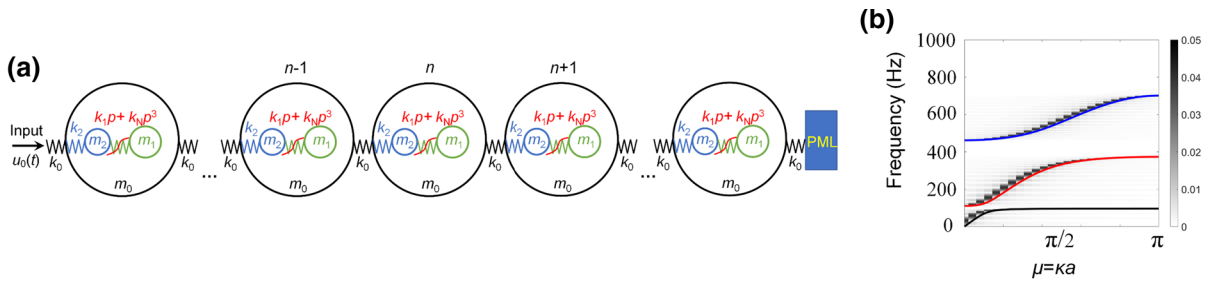

Fig. 1 Metamaterials model. **a** Schematic of the periodic triatomic chain. **b** Linear dispersion curves of the model calculated by analytical and numerical methods ($k_N = 0$). The solid curves are analytical results, and the gray shading regions are numerical results

wave propagation of this strongly nonlinear metamaterials model. As shown in Fig. 1, a unit cell contains three oscillators with respective masses m_0, m_1 and m_2 interconnected by different springs. As such, nonlinearity can appear between m_1-m_2, m_0-m_2 or m_0-m_0, which will alter the wave propagation. Before considering other cases, we take the case with nonlinearity between m_1 and m_2 as an example to demonstrate the methods and show typical phenomena. More specifically, cubic stiffness nonlinearity $k_1p + k_Np^3$ is considered, with k_1 and k_N denoting the linear and nonlinear stiffness coefficients, respectively.

In this case, the neighboring oscillators m_0 in the primary chain are coupled through linear stiffness k_0, and m_2 couples to m_0 through a linear stiffness k_2. Damping is not considered. The displacements of m_0, m_1 and m_2 are u_n and y_n and z_n, respectively, and $p_n = y_n - z_n$. Thus, the equations of motion for the nth unit cell write:

$$\begin{cases} m_0\ddot{u}_n = k_0(u_{n+1} + u_{n-1} - 2u_n) + k_2(z_n - u_n) \\ m_1\ddot{y}_n = -k_1p_n - k_Np_n^3 \\ m_2\ddot{z}_n = -k_2(z_n - u_n) + k_1p_n + k_Np_n^3 \end{cases} \tag{1}$$

Mindful of the possible deficiencies of the Bloch–Floquet theorem in dealing with nonlinear systems [39], we still use it to solve the above system to get the dispersion curves and then clarify its limitations hereafter. According to the Bloch–Floquet theorem, $u_{n+1} = u_ne^{-i\kappa a}$, $u_{n-1} = u_ne^{i\kappa a}$, $\kappa a = \mu \in [0, \pi]$, the motion equation of the nth unit cell can be written as:

$$\mathbf{M}\ddot{\mathbf{X}} + \mathbf{K}\mathbf{X} + \mathbf{K_N}\mathbf{X}^3 = 0 \tag{2}$$

where

$$\mathbf{M} = \begin{bmatrix} m_0 & 0 & 0 \\ 0 & m_1 & m_1 \\ 0 & 0 & m_2 \end{bmatrix},$$

$$\mathbf{K} = \begin{bmatrix} k_2 - k_0(e^{-ika} + e^{ika} - 2) & 0 & -k_2 \\ 0 & k_1 & 0 \\ -k_2 & -k_1 & k_2 \end{bmatrix},$$

$$\mathbf{K_N} = \begin{bmatrix} 0 & 0 & 0 \\ 0 & k_N & 0 \\ 0 & -k_N & 0 \end{bmatrix} \text{ and } \mathbf{X} = \begin{bmatrix} u_n \\ p_n \\ z_n \end{bmatrix}$$

Natural frequencies of individual oscillators before they are coupled together are denoted by $\omega_i = \sqrt{k_i/m_i} = 2\pi f_i$, $i = 0, 1, 2$. Taken from a recent experimental configuration [39], parameters used in the simulation are: $a = 1$, $m_0 = 5.8$, $m_1 = 2.1$, $m_2 = 2$ g; $f_0 = 322$, $f_1 = 100$, and $f_2 = 390.6$ Hz. We took $k_N = 1 \times 10^{13}$ N/m^3 to show the nonlinear phenomena.

In our previous work [38], we have performed a comparison among different methods, namely equivalent method, homotopy analysis method, perturbation approach and harmonic balance method to assess their suitability for the study of the dispersion properties in strongly nonlinear acoustic metamaterials. The equivalent method only allows for a rough estimate of the dispersion and reaches its limit when the nonlinearity become very strong. The perturbation approach, however, is only applicable to weakly nonlinear periodic models. By contrast, harmonic balance method and homotopy analysis method are, in principle, good candidates for analyzing both weak and strong nonlinearities, although the latter is more complicated. Thus, we opt for the harmonic balance

method in this work. Here, we adopt the first-order harmonic balance method to solve Eq. (2) by assuming the solution as

$$\mathbf{X} = \mathrm{A}\sin(\omega t) \tag{3}$$

in which $\mathbf{A} = [A_0,\ A_{12},\ A_2]^{\mathrm{T}}$ with A_0, A_{12} and A_2 standing for the amplitudes of u_{n}, p_{n} and z_{n}, respectively; $\omega = 2\pi f$. Substituting Eq. (3) into (2) and balancing the coefficients of $\sin(\omega t)$ give:

$$[K - \omega^2 M]\mathrm{A} + \frac{3}{4}K_N\mathrm{A}^3 = 0 \tag{4}$$

By specifying A_0 for a given wave number $\mu = \kappa a \in [0, \pi]$, the eigenfrequency ω and the eigenvector $[A_0, A_{12}, A_2]^{\mathrm{T}}$ can be obtained from Eq. (4). A_1 is the amplitude of y_n, and $A_1 = A_{12} + A_2$. The normalized eigenvector $[A_0,\ A_1,\ A_2]^{\mathrm{T}}/A_0$ represents the corresponding wave mode (i.e., the vibration mode of the periodic unit cell).

Meanwhile, a numerical approach is adopted to calculate the dispersion curves. The numerical model consists of 2000 triatomic cells. An optimized perfect matching layer is connected to the right end of the chain to suppress possible wave reflection. A displacement excitation, $u_0(t)$, is imposed at the left end of the chain. $u_0(t)$ is a chirp harmonic wave whose frequency increases from 0 to 1000 Hz within 1 s. It takes more than 1 s for the wave to reach the metacells in the far field. Thus, the duration of the response is 2 s (i.e., the simulation time), which is enough for the first 500 metacells to endure the wave propagation process (in the present case, we just involve the calculation of the first 200 metacell). Once the time-domain response $u(n, t)$ for the nth cell is extracted, we conduct a 2D fast Fourier transform (2DFFT) to obtain the 2D frequency spectrum:

$$V(\mu, f) = \sum_{n=2}^{N-1}\int_0^T u(n,t)e^{-j(\mu n+\omega t)}\mathrm{d}t \tag{5}$$

where N denotes the number of cells used in the 2DFFT, and $T = 2$ s denotes the simulation time. While transforming the time-domain signal into frequency domain by using 2DFFT, the space variable n is transformed into the wave number μ. Therefore, the spectrum $V(\mu, f)$ represents the dispersion curves. A larger N offers a higher resolution of the wave vector μ in $V(\mu, f)$. However, N cannot be excessively large due to the self-adaptive band structure (see Appendix).

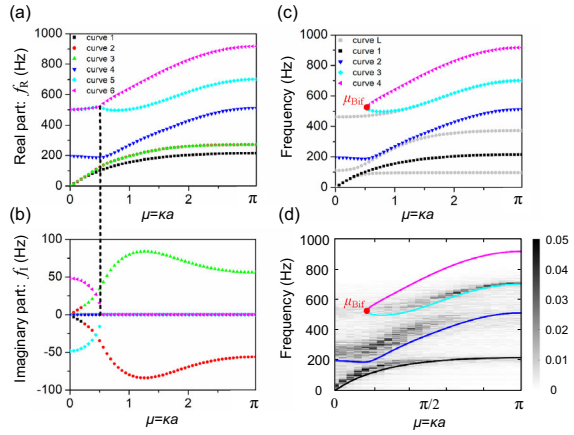

Fig. 2 Dispersion curves of nonlinear metamaterials model with $A_0 = 5$ μm. **a** and **b** The real part f_{R} and imaginary part f_{I} of the curves. There are 6 curves. The corresponding curves in the upper and lower panels use the same type of lines. **c** Curves only with real numbers (i.e., $f_{\mathrm{I}} = 0$). Herein, the gray curves are the linear results. **d** Numerical and analytical dispersion curves

Here, the 2DFFT is conducted using the signals of the first 50 cells ($N = 50$) counting from the excitation position.

To validate the method, we calculate the dispersion curves of the corresponding linear metamaterials model (with $k_{\mathrm{N}} = 0$). As shown in Fig. 1b, the analytical and numerical dispersion curves agree well with each other. This particular configuration entails a Bragg bandgap (from 700 Hz on) and two locally bandgaps LR1 (96.1, 110.4) Hz and LR2 (373.4, 462) Hz.

3 Salient properties of nonlinear band structure

In this section, we explore typical dispersion properties of the model with $A_0 = 5$ μm, as shown in Fig. 2. The complex frequency solutions, $f = \omega/2\pi = f_{\mathrm{R}} + \mathrm{i}f_{\mathrm{I}}$, are obtained for any given wave vector μ, where f_{r} and f_{I} denote the real and imaginary parts, respectively. As shown in Fig. 2a and b, the harmonic balance solution presents six dispersion curves, instead of three in the linear model. Several interesting phenomena are noteworthy. All solutions on curves 1 and 4 are real numbers ($f_{\mathrm{I}} = 0$), which shift upwards relative to the linear curves, and the part in $\mu \in [0, 0.5]$ on curve 4 is also uplifted. Curves 2 and 3 correspond to the conjugate solutions with very large f_{I}. Interestingly, curves 5 and 6 feature a bifurcation at the

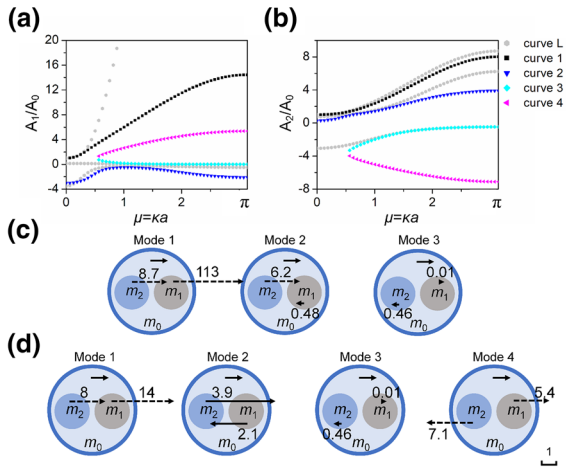

Fig. 3 Normalized vectors and wave modes of the linear and nonlinear metamaterials. $A_0 = 5$ μm. **a** and **b** Normalized vectors A_1/A_0 and A_2/A_0 with respect to the wave number μ, respectively. Herein, curve L and curves 1–4 denote the linear and nonlinear cases, respectively. Colors used in (**a**) and (**b**) correspond to the curves with the same colors in Fig. 2(c). **c** and **d** wave modes for linear and nonlinear metamaterials at $\mu = \pi$, respectively. Mode *j* corresponds to curve *j* in (**a**) and (**b**). The length and the direction of arrows denote the generalized length A_i/A_0 and the corresponding phase (positive or negative), respectively. Numbers (value = A_i/A_0,) are labeled near arrows. The arrow length of m_0 is set to 1, and other arrows are presented relative to 1. Some arrows are dashed lines as the value A_i/A_0 is so large, which are truncated in length and presented by dashed arrows

specific wave vector μ_{Bif} ($\mu_{\mathrm{Bif}} = 0.56$ for the present case with $A_0 = 5$ μm).

In $\mu \in [0, \mu_{\mathrm{Bif}}]$, solutions on curves 5 and 6 are conjugate with large f_{I}, while in $\mu \in [\mu_{\mathrm{Bif}}, \pi]$, they bifurcate into two branches with zero imaginary part $f_{\mathrm{I}} = 0$. This means the two dispersion curves degenerate at μ_{Bif}, a degeneration induced by nonlinearity. Expressing the wave in the nonlinear lattice as $U(x,t) = A\exp(\omega t - kx)$, any solution component with large $f_I \neq 0$ implies a rapid attenuation of the wave. Therefore, we can remove these solutions from the band structure and finally obtain four dispersion curves shown in Fig. 2c. Now they are re-numbered as curves 1 to 4. As shown in Fig. 2c, the numerical solution is consistent with the analytical one. Some differences appear due to the wave amplitude which varies in the chain (i.e., in the analytical solution, all amplitudes in $n < 50$ are set to A_0, but actually it is not a constant across the units). Importantly, the numerical curve 3 is also noncomplete—the part in [0, μ_{Bif}] disappears, as the analytical curve does. This confirms the degeneration of the nonlinear band structure. Meanwhile, the numerical results fail to present curve 4 predicted by the analytical solution. The following study will clarify its observation.

On the other hand, the normalized vector $[A_0, A_1, A_2]^{\mathrm{T}}/A_0$ from the analytical solution represents a wave mode. The normalized displacements of m_1 (A_1/A_0) and m_2 (A_2/A_0) are shown in Fig. 3a and b, respectively. The wave modes at $\mu = \pi$ include the phase between different oscillators and their respective vibration displacement amplitudes. They are important metrics of local resonances and scattering, showing the essence of the bandgaps. As shown in Fig. 3c, d, three circles represent the oscillators m_0, m_1 and m_2; and vectors represent their wave modes. Similarly, the direction and the length of a vector denote the phase and displacement, respectively.

For the linear metamaterials in Fig. 3c, mode 1 is the local resonance of m_1; mode 2 is the local resonance of both m_1 and m_2 (vibrating in phase), respectively; in mode 3, the displacements of m_1 and m_2 are tiny relative to that of m_0, which belongs to the Bragg scattering of m_0 at the periodic lattice interface. The observed resonance and scattering inform on the well-known mechanisms of locally resonant bandgap and Bragg bandgap in linear metamaterials [6, 7]. For the nonlinear metamaterials in Fig. 3d, modes 1 and 2 still show typical local resonances, but A_1/A_0 in mode 1 and A_2/A_0 in mode 2 decrease greatly relative to the corresponding linear modes and curves (see Fig. 3a, b). A_1/A_2 in modes 1 and 2 change from 13 and 0.08 in the linear metamaterials, further to 1.75 and 0.54 in the nonlinear metamaterials, which suggests that both m_1 and m_2 take part in the local resonance in the nonlinear metamaterials. Mode 3 remains nearly unchanged at $\mu = \pi$ for $A_0 = 5$ μm. Moreover, the nonlinear metamaterials possesses an extra mode 4 owing to an extra dispersion curve 4 in Fig. 2c. In this mode, m_0 and m_2 vibrate with opposite phase, $|A_2| > A_0$, but $|A_2| > |A_1|$, which indicates an inverse resonance of m_2 (different from the resonance of modes 1 and 2). More features of this mode will be scrutinized in the following. These phenomena show the band degeneration and mode transition in nonlinear metamaterials. Next, we will study their evolution process and the underlying mechanisms.

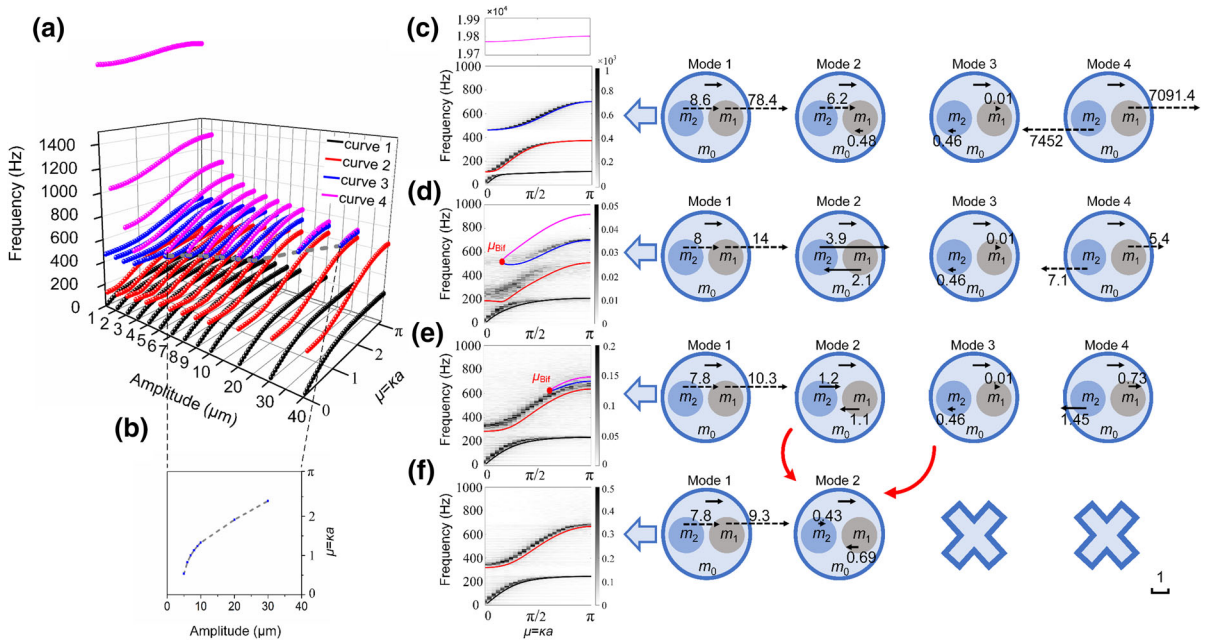

Fig. 4 Evolution of dispersion curves and wave modes with increasing incident amplitude A_0. **a** Overall view of analytical dispersion curves varying with increasing amplitude A_0. **b** Trace of bifurcation in (**a**). **c**–**f** Four typical cases showing their analytical and numerical dispersion curves and wave modes; **c** Case-1: weak nonlinearity (A_0 = 0.1 μm), **d** Case-2: moderate nonlinearity (A_0 = 5 μm), **e** Case-3: strong nonlinearity (A_0 = 30 μm), **f** Case-4: stronger nonlinearity (A_0 = 40 μm)

4 Evolutionary process of the nonlinear band structure

Figure 4 shows the variation process of the dispersion curves and wave modes when A_0 increases. Interestingly, the harmonic balance method predicts 4 dispersion curves for weakly nonlinearity in mathematics. With increasing A_0, curves 3 and 4 (the blue and pink ones) disconnect for $A_0 \to 0$, connect at $\mu = 0$ for $A_0 = 4.4$ μm, and then degenerate (becomes incomplete) and bifurcate at $0 < \mu_{\text{Bif}} < \pi$. At last, curves 3 and 4 disappear under very strong nonlinearity: only two curves are left behind. Moreover, the behaviors manifested by curves $1 \sim 4$ are accurately confirmed by numerical results.

We take four typical cases to explain the aforementioned degeneration and bifurcation process, as shown in Fig. 4c–f. When nonlinearity is negligibly weak (the case A_0 = 0.1 μm in Fig. 4c), four dispersion curves are present mathematically. Curves $1 \sim 3$ are all below 700 Hz while curve 4 appears in 19,810–19,790 Hz at A_0 = 0.1 μm. Except for curve 4, all other analytical curves agree with those from simulations that are identical with the linear band structure. Different from modes 1 and 2, curve 4 represents the reverse resonances of m_1 and m_2, in which A_2/A_0 and A_1/A_0 abnormally reach − 7452 and 7091 for A_0 = 0.1 μm, respectively. As the nonlinear force is $k_1(A_1 - A_2) + k_N(A_1 - A_2)^3$, this means that this nonlinearity should become extremely strong, contradicting to the small input A_0 = 0.1 μm. Our simulation method by inputting wave energy $u_0(t)$ from the left end of the chain fails to get this curve that matches the analytical result, from weak to moderate nonlinearity range in Fig. 4d. Presenting this abnormal mode in simulation may requires accurately controlling the phase and displacement of all oscillators. In this paper, we will focus on curves $1 \sim 3$ to clarify other phenomena and mechanisms.

With further enhanced nonlinearity by increasing A_0, as shown in Fig. 4a, curve 1 (the black one) shifts upwards from (0, 173.3) to (0, 242.6) Hz, and curve 2 (the red one) from (118.6, 379.8) to (313.4, 661.3) Hz. This leads to the modulation of bandgap 1 between curves 1 and 2: it first becomes blind at $A_0 \approx 1$ μm and then opens again when $A_0 > 8$ μm. The wave modes inform on the mechanism. By increasing A_0 from 0.1 to 40 μm, A_1/A_2 decreases from 9.1 (in Fig. 4) to 1.2.

This suggests a change in the dominant mechanism of bandgap 1 from "the local resonance of m_1" to "the synchronous local resonance of m_1 and m_2".

The shifting of curve 2 is highly relevant to the degeneration of curves 3 and 4 in this process. The bifurcation point μ_{Bif} of curves 3 and 4 increases from 0 to π as A_0 increases from 4.4 to 37.8 μm (see Fig. 4b). Meanwhile, curves 3 and 4 shorten, merge and disappear at last. However, the cutoff frequency of curve 3 (when it exists) remains almost unchanged. The merging takes place as a result of the downward shifting of curve 4. Moreover, the cutoff frequency of curve 2 increases just right to the cutoff frequency of curve 3. "Disappearance of curve 3" occurs at the same A_0 as "the arriving of curve 2". This alludes to an interesting suspicion: curve 2 takes over the role of curve 3 when enhancing nonlinearity from weak to extremely strong state. Sure enough, an analysis on the variation of modes 2 and 3 would confirm this. As shown in Fig. 4c–f, when A_0 increases from zero to 30 μm, the phases of m_1 and m_2 remain opposite, $|A_2/A_1|$ changes slightly, but A_2/A_0 decreases from 6.2 to 1.2, and A_2/A_0 finally decreases to 0.43 at A_0 = 40 μm. In the whole process, mode 3 nearly remains invariant. The only difference between mode 2 and mode 3 at A_0 = 40 μm is the sign of A_2/A_0. As $A_2/A_0 \to 0$, the positive or negative signs negligibly influence the wave dynamics. Therefore, same with mode 3, mode 2 at A_0 = 40 μm represents the Bragg scattering. This means all modes 2, 3 and 4 merge and behave as Bragg scattering under very strong nonlinearity. Thus, although the shape of curve 2 is not significantly altered, the mechanism for the response changes from the "local resonance of m_1 and m_2" to "scattering between m_0". In this process, the second locally resonant bandgap between curves 2 and 3 becomes blind at $A_0 \approx 4.3$ μm but it does not appear again.

Overall, with enhancing nonlinearity, three bandgaps retreat and degenerate into two bandgaps owing to the merging of modes 2, 3 and 4. In other words, the nonlinear metacell transforms a 3-DoF unit cell to a 2-DoF one under strong nonlinearity. The observed dimensionality reduction with enhanced nonlinearity is unique and specific to strongly nonlinear metamaterials model. This property will be explored in other strongly nonlinear systems hereafter so that some

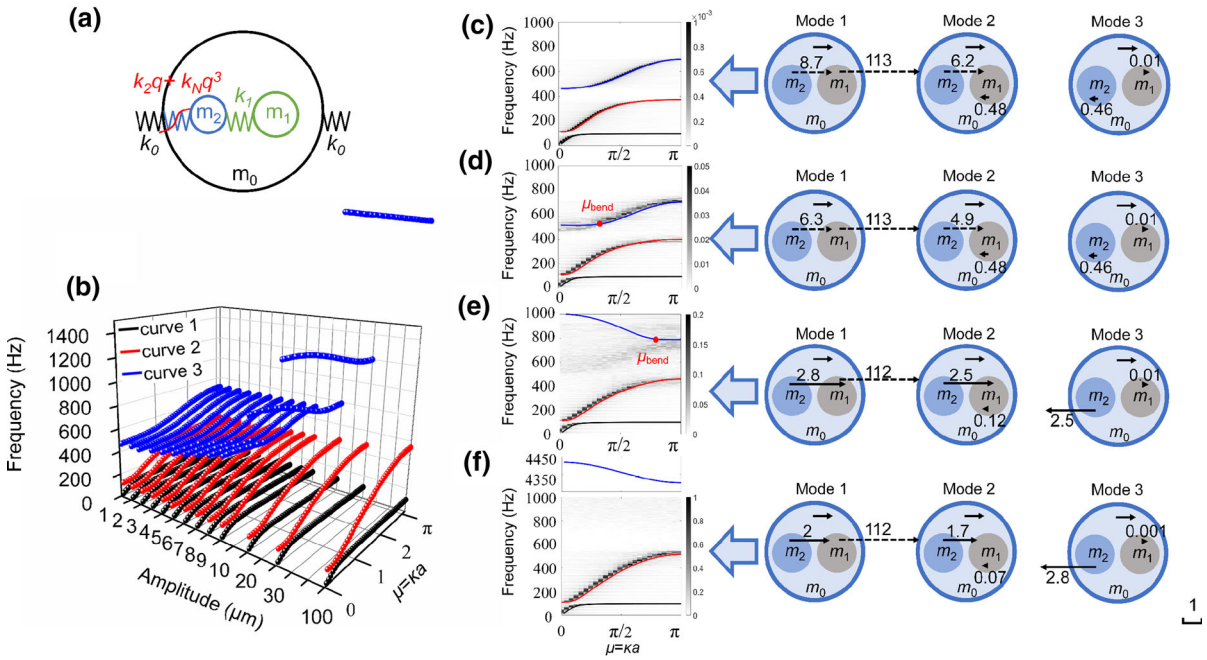

Fig. 5 Evolution of dispersion curves and wave modes with increasing incident amplitude A_0 when the position of nonlinearity is exchanged. **a** Triatomic metacell. **b** Analytical dispersion curves with respect to increasing amplitude A_0. **c**–**f** Four typical cases showing their analytical and numerical dispersion curves and wave modes; **c** Case-1: weak nonlinearity (A_0 = 0.1 μm), **d** Case-2: moderate nonlinearity (A_0 = 5 μm), **e** Case-3: strong nonlinearity (A_0 = 30 μm), **f** Case-4: very strong nonlinearity (A_0 = 100 μm)

universal relations be extracted and established in Sect. 5.

5 Evolution of the band structure in other typical models

Here, we consider three other typical models to show the generality of the band generation and degeneration phenomena observed above. In the first model, the position of the nonlinear component is changed and placed between m_2 and m_0, while the connection between m_1 and m_2 becomes linear, as shown in Fig. 5a. In the second model, both connections are nonlinear to represent a complex nonlinear coupling case, as shown in Fig. 8a. Moreover, unlike the above three models in which nonlinearity exists between local resonators, we investigate the fourth model shown in Fig. 10a, in which the springs connecting the rings of the primary resonator m_0 become nonlinear.

5.1 Nonlinearity with exchanged position

Denoting the displacements of m_0, m_1 and m_2 by u_n, y_n and z_n, respectively, and assuming $q_n = z_n - u_n$, the equations of motion in a metacell shown in Fig. 5a write:

$$\begin{cases} m_0\ddot{u}_n = k_0(u_{n+1} + u_{n-1} - 2u_n) + k_2 q_n + k_2 q_n^3 \\ m_1\ddot{y}_n = -k_1(y_n - z_n) \\ m_2\ddot{z}_n = k_1(y_n - z_n) - k_2 q_n - k_N q_n^3 \end{cases} \tag{6}$$

Following the same analytical and numerical procedure as detailed in Sect. 3, we calculate the corresponding dispersion curves and wave modes. Figure 5b shows the variation of the dispersion curves and that of the wave modes when increasing the incident amplitude A_0. Unlike the band structure in Fig. 4a, only three dispersion curves appear irrespective of the amplitude value A_0. When increasing A_0, the portion $\mu \in [0, \mu_{\text{bend}}]$ on curve 3 bends upwards, with the point μ_{bend} shifting from 0 to π. At last, the entire curve 3 shifts upwards to a high frequency under very strong nonlinearity. Moreover, the variation trends manifested by curves 1 $\sim$ 3 are also confirmed by numerical results.

We also examine four typical cases to explain the aforementioned bending and shifting phenomena in

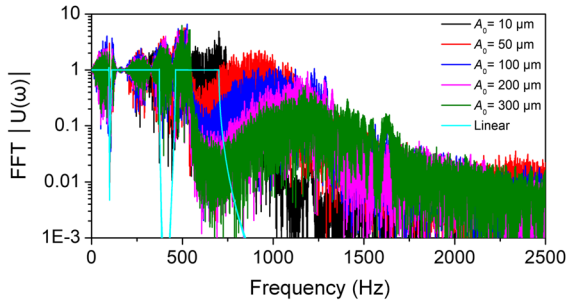

Fig. 6 Normalized frequency spectra of the response of the 5th metacell under a chirp wave excitation in the range of 0–2500 Hz. **a** Triatomic metacell. **b** The frequency spectra were obtained by the fast Fourier transform (FFT)

Fig. 5c–f. Unlike the nonlinear system discussed in Sect. 4.1, no degeneration of curves is noticed. Curve 1 (the black one) shifts upwards from (0, 97.2) to (0, 99.1) Hz and curve 2 (the red one) from (110.8, 404.2) to (111.2, 515.3) Hz. The observed changes are consistent with those obtained from simulations as a result of nonlinearity enhancement. Mode 1 always behaves as the local resonance of m_1 although A_2/A_0 decreases slightly. By contrast, A_2/A_0 in mode 2 decreases from 6.2 at $A_0 = 0.1$ μm to 1.7 at $A_0 = 100$ μm ($A_2/A_0 \to 1$). This happens because the stiffness between m_2 and m_0 expressed by $k_1 + 3k_N(A_2 - A_0)^2$ becomes much larger than its linear counterpart k_1, and thus m_2 is "fixed" onto m_0. As a result, mode 2 transforms from the local resonance of m_2 to the Bragg scattering between the "merged" mass $m_0 + m_2$.

Mode 3 for small input represents the Bragg scattering, but A_2/A_0 increases from 0.46 to 2.8 under strong nonlinearity. Therefore, curve 3 represents the high frequency resonance of m_2 under the strong nonlinearity. Meanwhile, curve 3 agrees well with the simulated one in the weak nonlinearity case. However, when nonlinearity increases to the moderate case, the portion $\mu \in [0, \mu_{\text{bend}}]$ on curve 3 disappears in simulation. The frequency spectrum covering curve 3 at $A_0 = 30$ μm is continuous, which actually indicates the occurrence of chaotic responses [22].

When nonlinearity becomes extremely strong, the entire curve 3 (not only the part in $\mu \in [0, \mu_{\text{bend}}]$) shifts to a high frequency range, although it is difficult to find such a curve in the 2DFFT simulation. Fortunately, we can still find this curve on the first 5 metacells close to the excitation, as shown in Fig. 6.

It is obvious that the third passband for curve 3 shifts from ∼ 600 Hz to ∼ 1250 Hz from linear state to the strongly nonlinear state with A_0 = 300 μm. Therefore, this curve does exist, but it appears only near the incident source region and its frequency range deviates from the analytical solution. A plausible reason is attributed to the self-adaptive band structure (see Appendix). We note that curve 3 under large input appears in the bandgap of its linear counterpart. As demonstrated earlier [39], the band structure of the nonlinear metamaterial is self-adaptive. Due to the chaotic responses and harmonic generation, waves in the passband of nonlinear metamaterials still undergo attenuations as the propagation distance increases. Due to the amplitude-dependent property, an attenuated amplitude leads to a different band structure. The linear bandgap finally appears when the amplitude becomes small. For example, although curve 3 shifts to 1250 Hz for A_0 = 300 μm near the excitation source, it rapidly attenuates as the propagation distance increases. Moreover, though the incident amplitudes A_0 are 50, 100, 200 and 300 μm, the mean amplitudes at the 5th unit cell are much smaller, i.e., 23, 34, 54, and 90 μm. Thus, the numerical results deviate from the numerical results.

In short, although curve 3 does exist, its response disappears in an infinite chain, and the nonlinear system is converted from 3 to 2DoF systems with enhanced nonlinearity. Although the nonlinear systems in Sect. 4.1 and Sect. 5.1 both evolve from 3 to 2DoF systems when nonlinearity increases, they are different in principle. While the band degeneration in the former model undergoes shortening, merging of a dispersion curve but the first resonant bandgap is broadened; while the band degeneration in the latter model mainly features a curve shifting, response attenuation and a narrowing-down of the first resonant bandgap. Therefore, the dimensionality reduction in strongly nonlinear metamaterials model with enhancing nonlinearity may take place in different ways.

5.2 Complex nonlinear coupling

With the principle demonstrated in Sects. 4 and 5.1, one could surmise that if the two resonators all become nonlinear as Fig. 8a, the metacell would then evolve from 3DoF to a 1DOF system with enhanced nonlinearity. This is investigated here. The displacements of

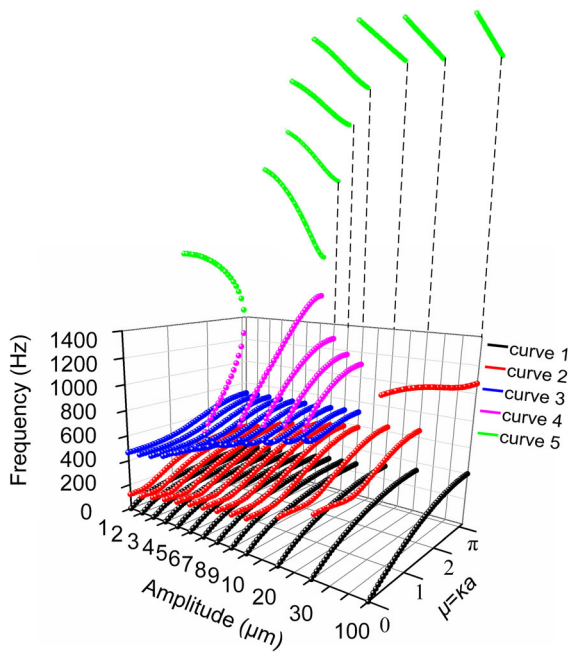

Fig. 7 Analytical dispersion curves with increasing amplitude A_0 in the complex nonlinear coupling case

m_0, m_1 and m_2 are u_n, y_n and z_n, respectively, $p_n = y_n - z_n$, $q_n = z_n - u_n$, and the equations of motion of in a metacell read:

$$\begin{cases} m_0\ddot{u}_n = k_0(u_{n+1} + u_{n-1} - 2u_n) + k_2 q_n + k_2 q_n^3 \\ m_1\ddot{y}_n = -k_1 p_n - k_N p_n^3 \\ m_2\ddot{z}_n = -k_2 q_n - k_N q_n^3 + k_1 p_n + k_N p_n^3 \end{cases} \tag{7}$$

Following the same analysis method in Sect. 3, Fig. 7 shows the variation of the dispersion curves and wave modes with respect to increasing incident amplitude A_0 in this complex nonlinear coupling case. This model features both type of the band degeneration phenomena discussed in Sects. 4 and 5.1. The harmonic balance method predicts 3 dispersion curves when nonlinearity is weak. Interestingly, curves 4 and 5 appear with increasing A_0 before bifurcating at $0 < \mu_{\mathrm{Bif1}} < \pi$. At last, curves 4 and 5 disconnect at $\mu = \pi$ under moderate nonlinearity and shift downwards and upwards, respectively. Then, similar to the degeneration process in the first model, curves 3 and 4 degenerate and bifurcate at $0 < \mu_{\mathrm{Bif2}} < \pi$. At last, curves 3 and 4 disappear under strong nonlinearity with only three curves left behind. When further increasing A_0, curve 2 shifts upwards, similar to that of

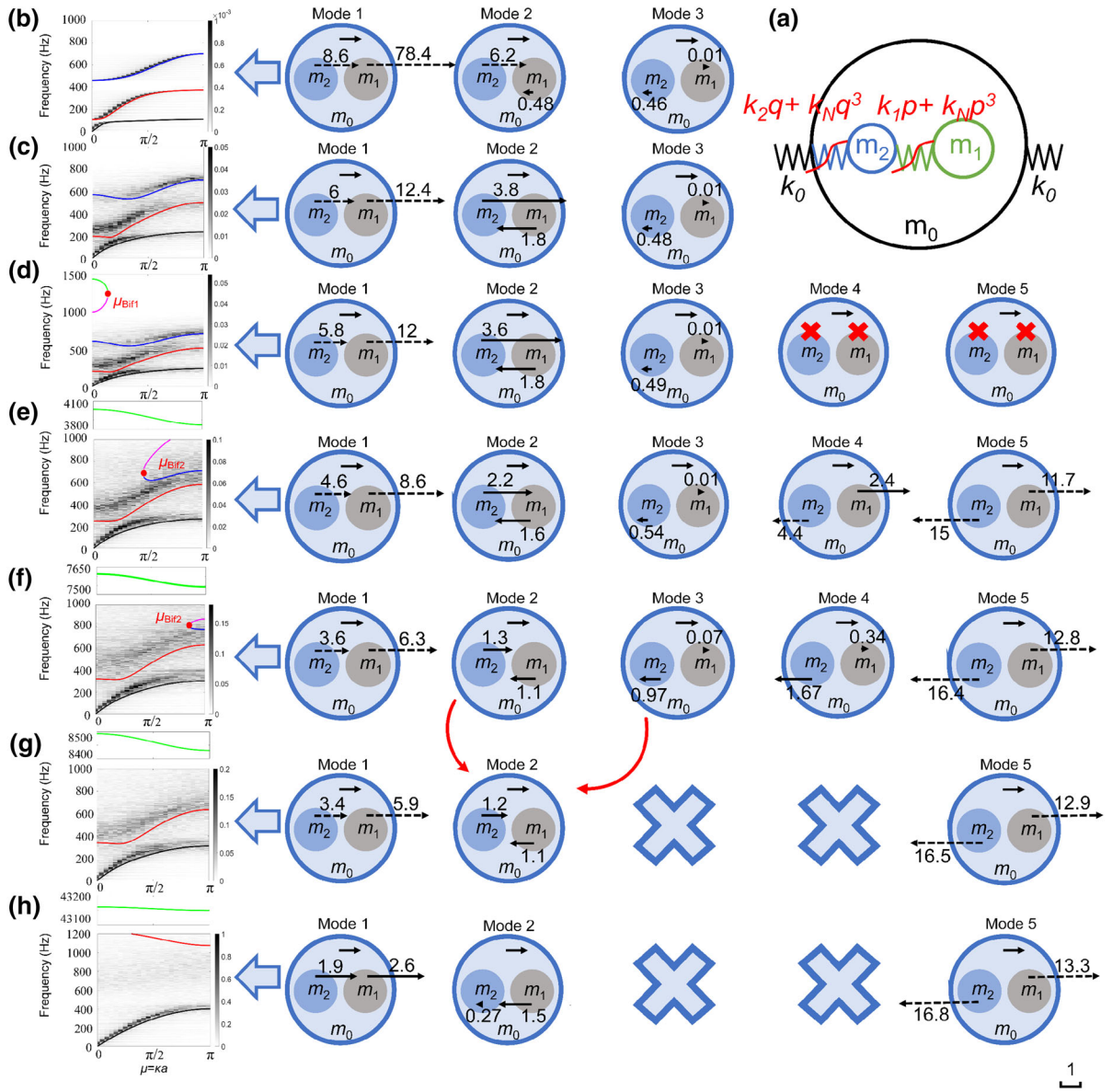

Fig. 8 Evolution of dispersion curves and wave modes with increasing incident amplitude A_0 in the complex nonlinear coupling case. **a** Triatomic metacell. **b–h** Seven typical cases showing their analytical and numerical dispersion curves and wave modes; (b) Case-1: weak nonlinearity (A_0 = 0.1 μm), **c** Case-2: moderate nonlinearity 1 (A_0 = 5 μm), **d** Case-3: moderate nonlinearity 2 (A_0 = 5.4 μm), **e** Case-4: strong nonlinearity 1 (A_0 = 10 μm), **f** Case-5: strong nonlinearity 2 (A_0 = 18 μm), **g** Case-6: strong nonlinearity 3 (A_0 = 20 μm) **h** Case-7: strong nonlinearity 4 (A_0 = 100 μm)

curve 3 discussed in Sect. 5.1. Moreover, the behaviors manifested by curves 1 ∼ 4 are accurately confirmed by the numerical results.

We take seven typical cases to investigate the behavior of dispersion curves and the evolution of wave modes in Fig. 8b–h. When nonlinearity is negligibly weak (the case A_0 = 0.1 μm in Fig. 8b), there exist three dispersion curves mathematically, and all analytical curves agree with those from the simulations, which are identical to the linear band structure. When nonlinearity evolves from moderate to strong (the cases A_0 = 5.4, 10 and 18 μm in Fig. 8d–f), complex changes take place. In short, curves 3 and 4 are highlighted by a "shortening, merging, and disappearance" process, similar to the first model in Sect. 4.1. At A_0 = 7 μm, curves 4 and 5 disconnect at

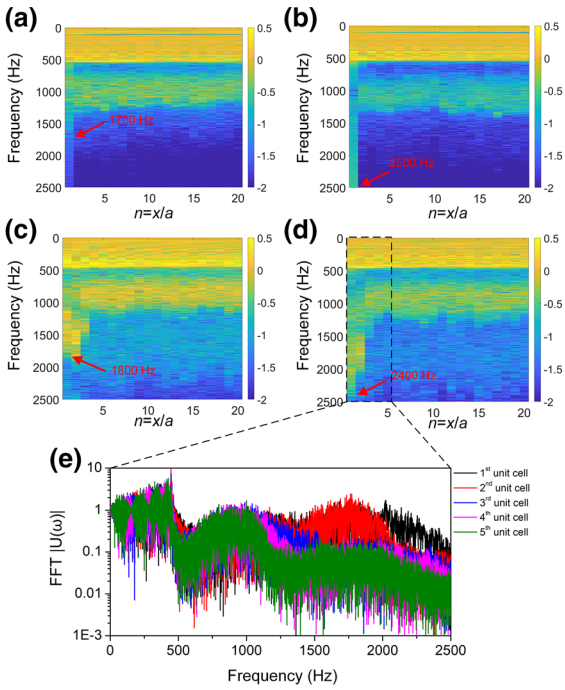

Fig. 9 Normalized amplitude Spectra of the nth metacell under a chirp wave excitation of 0–2500 Hz. **a**, **b** Results for the second model. **c**, **d** Results for the third model. **a**, **c** A_0 = 100 μm. **b**, **d** A_0 = 200 μm. The shade of color represents the amplitude spectra in the range of 0–2500 Hz. **e** Normalized frequency spectra in the first five cells near the incident source of (**c**), which is an example to understand (**c**)

$\mu = \pi$, but for $A_0 < 7$ μm, curves 4 and 5 have no wave mode at $\mu = \pi$ (i.e., they appear at $\mu = 0$ but cannot reach $\mu = \pi$).

Mode 4 degenerates from local resonance to Bragg scattering. Mode 5 shows that curve 5 always involve the reverse resonances of both m_1 and m_2, like the reverse resonance in Fig. 4, the simulation method also fails to present them. When nonlinearity is extremely strong (the case with A_0 = 100 μm in Fig. 8h), curve 2 cannot be found, but it can be confirmed in the detailed analysis, like the curve 3 of the second model in Sect. 5.1. We compare the spectra of the second and third models when A_0 = 100 and 200 μm in Fig. 9. When A_0 increases from 100 to 200 μm, the two passbands for curve 3 in the second model and for curve 2 in the third model both shift to high frequencies. Particularly in the first cell, the passbands for curve 3 in the second model cover 0–2500 Hz instead of 0–1700 Hz, and passbands for curve 2 in the third model cover 0–2400 Hz instead of 0–1800 Hz. Therefore, curves 3 and 2 in the second and third models do exist, and they do appear only near the incident source as demonstrated in Sect. 5.1.

In light of the conclusions reached in Sects. 4 and 5.1, the evolution of the band structures undergoes two stages: (1) shortening and merging ($A_0 < 20$ μm) and (2) shifting and response disappearance ($A_0 > 20$ μm).

In the shortening and merging stage, as shown in Fig. 8b–g, curves 2, 3 and 4 follow the same evolution as those of curves 2,3 and 4 in Sect. 4.1. The "disappearance of curve 3" catches up with "the arrival of curve 2", but at different frequencies. This difference shows that there is a competing mechanism between the two nonlinearities: $k_N(A_2 - A_0)^3$ and $k_N(A_2 - A_1)^3$, i.e., depending on their respective dominance nonlinearity level.

In the shifting and response disappearance stage, as shown in Fig. 8g–h, for mode 1 on curve 1, A_1/A_0 decreases from 5.9 to 2.6, and A_2/A_0 from 3.4 to 1.9, i.e., both approach to the state $A_1 = A_2 = A_0$. This means that m_0, m_1 and m_2 can be considered as a merged oscillator with a total effective mass $m_0 + m_1 + m_2$. Therefore, the mechanism for the first bandgap evolves from the synchronous resonance of m_1 and m_2 to the Bragg scattering between the merged oscillator. Similarly, mode 2 also evolves from the local resonance of m_2 to Bragg scattering. Moreover, mode 3 nearly remains intact, like those discussed in Sect. 4.1. Therefore, in this model, except for curve 5, all other modes evolve to Bragg scattering under very strong nonlinearity. The unit cell is gradually converted from a 3DoF system to a 2DoF, and finally to a 1-DoF system.

5.3 Nonlinearity in the primary chain

In the above three models, the dimension reduction and the band degeneration depend on the nonlinear coupling inside every metacell instead of between metacells. One might also be interested in investigating the influences of nonlinearity in the primary chain between metacells. Here we inspect the band structure of this kind of model, as shown in Fig. 10a. The equations of motion of a metacell read:

$$\begin{cases} m_0\ddot{u}_n = k_0(u_{n+1} + u_{n-1} - 2u_n) + k_N(u_{n+1} - u_n)^3 + k_N(u_{n-1} - u_n)^3 + k_2(z_n - u_n) \\ m_1\ddot{y}_n = -k_1(z_n - y_n) \\ m_2\ddot{z}_n = k_1(y_n - z_n) + k_2(u_n - z_n) \end{cases} \tag{8}$$

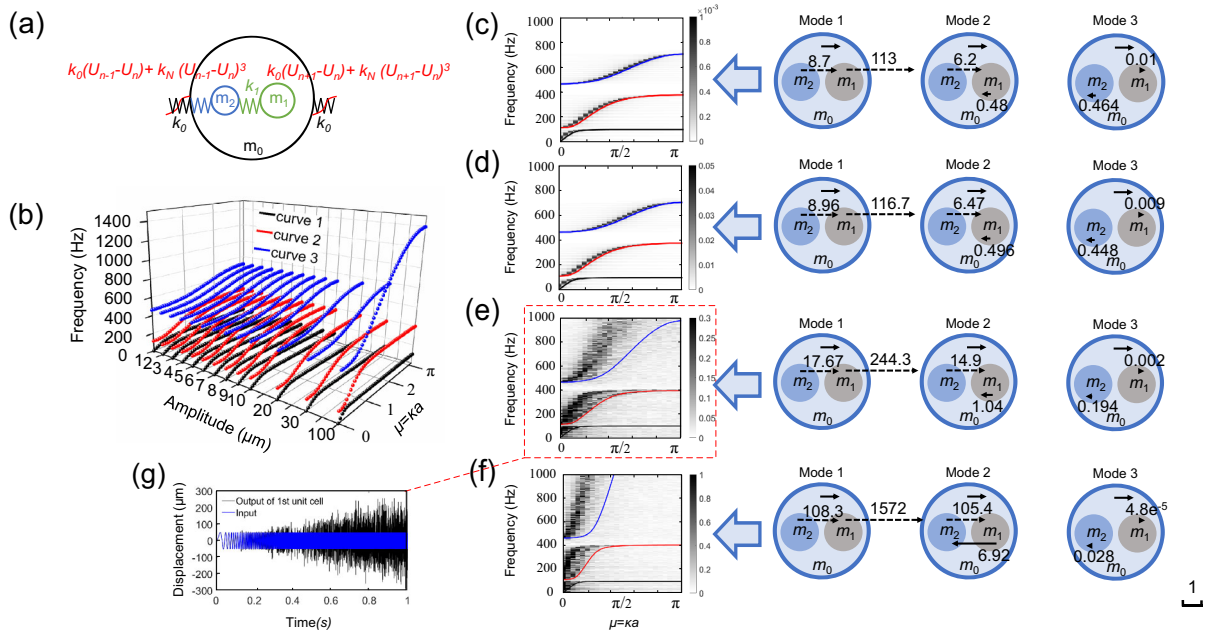

Fig. 10 Evolution of dispersion curves and wave modes with increasing incident amplitude A_0 when nonlinearity appears in the primary chain. **a** Metacell. **b** Analytical dispersion curves with respect to increasing amplitude A_0. **c**–**f** Four typical cases showing their analytical and numerical dispersion curves and wave modes; **c** Case-1: weak nonlinearity (A_0 = 0.1 μm), **d** Case-2: moderate nonlinearity (A_0 = 5 μm), **e** Case-3: strong nonlinearity (A_0 = 30 μm), **f** Case-4: very strong nonlinearity (A_0 = 100 μm). **g** Time domain of the excitation wave and the output wave of the first cell in case-3

All resonators inside the metacell are linear. Note we have to adopt a different way to use Bloch–Floquet theorem when the neighboring oscillators m_0 are coupled through nonlinear force. The wave in the nonlinear lattice is expressed as:

$$U(x,t) = \frac{1}{2}U\left[e^{i(kx+wt)} + e^{-i(kx+wt)}\right] \tag{9}$$

According to the Bloch–Floquet theorem, the Bloch wave considering the periodic boundary condition can be written as:

$$U(x+R,t) = \frac{1}{2}U[e^{ikR}e^{i(kx+wt)} + e^{-ikR}e^{-i(kx+wt)}] \tag{10}$$

where $R = na$. Thus, one has:

$$\begin{aligned}\Delta =& U(x+R,t) - U(x,t)\\ =& \frac{1}{2}U\left[(e^{ikR}-1)e^{i(kx+wt)} + (e^{-ikR}-1)e^{-i(kx+wt)}\right]\end{aligned} \tag{11}$$

and

$$\begin{aligned}\Delta^3 =& \frac{1}{8}U^3[(e^{ikR}-1)^3e^{3i(kx+wt)} + (e^{-ikR}-1)^3e^{-3i(kx+wt)}\\ &+ 3(-e^{2ikR} + 3e^{ikR} + e^{-ikR} - 3)e^{i(kx+wt)}\\ &+ 3(-e^{-2ikR} + 3e^{-ikR} + e^{ikR} - 3)e^{-i(kx+wt)}]\end{aligned} \tag{12}$$

when neglecting the third-order harmonic terms $e^{-3i(kx+wt)}$, Eq. (12) can be written as:

$$\begin{aligned}\Delta^3 \approx& \frac{3}{8}U^3[(-e^{2ikR} + 3e^{ikR} + e^{-ikR} - 3)e^{i(kx+wt)}\\ &+ (-e^{-2ikR} + 3e^{-ikR} + e^{ikR} - 3)e^{-i(kx+wt)}]\end{aligned} \tag{13}$$

Therefore, $k_N(u_{n+1} - u_n)^3 + k_N(u_{n-1} - u_n)^3$ can be written as:

$$\begin{aligned}&k_N(u_{n+1}-u_n)^3 + k_N(u_{n-1}-u_n)^3\\ &= \frac{3}{4}k_N\left[-e^{2ika} - e^{-2ika} + 4e^{ika} + 4e^{-ika} - 6\right]u_n^3\cos(kx + \omega t)\end{aligned} \tag{14}$$

Then, we adopt the first-order harmonic balance method as shown in Sect. 3 to get the band structure of this model like Fig. 5b. Only three dispersion curves appear in Fig. 10b. We also examine the four typical cases to explain the observed phenomena in Fig. 10c–f. The variation trends from the analytical results are still consistent with the 2D FFT results. The difference, however, becomes larger under strong nonlinearity, mainly because the true wave amplitude in the numerical response is higher than the preset amplitude value A_0 used in the analytical approach, as shown in Fig. 10g. Thus, the numerical dispersion curve is sharper.

In this model, increasing A_0 does not lead to the shortening of the dispersion curves and the merging of the bandgaps. The cutoff frequencies of curves 1 and 2 almost remain the same because their locally resonant frequencies remain unchanged. However, all rising parts on the dispersion curves become steeper for larger amplitude, and the cutoff frequency of curve 3 quickly shifts to higher frequencies. This effect can be quantified by the group velocity, calculated by the slope of dispersion curves $d\omega/d\kappa$. As shown in Fig. 11, an increase in the amplitude results in a drastic rise in the group velocity near $\kappa a = \pi/2$, especially for curve 3. Moreover, we also inspect the wave modes. Despite a significant change in A_2/A_0 and A_1/A_0, mode 1 always behaves as the local resonance of m_1; mode 2 that of m_2, and mode 3 as Bragg scattering. Thus, the mechanisms of bandgaps remain.

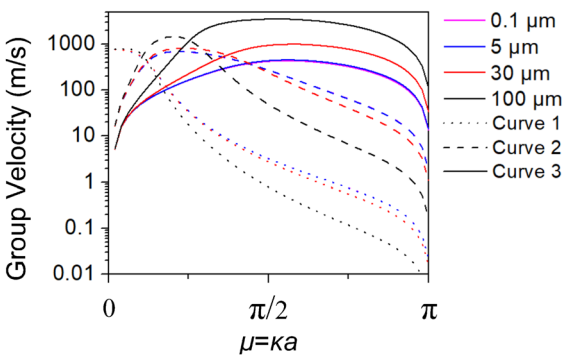

Fig. 11 Group velocity of curves 1 2 and 3 in case-2,3,4

This analysis shows that the influence of nonlinearity in the primary chain mainly exhibits a change in the group velocity of dispersion curves. The dimension, wave modes and the initial frequency of the locally resonant bandgap basically remain intact.

5.4 Summery

We summarize the evolution processes of the dispersion curves in the four metamaterials models in Fig. 12. The dispersion curves of nonlinear metamaterials may bifurcate at a wave vector for given wave amplitude; the curves may degenerate (i.e., shorten, merge or disappear) when the excitation amplitude increases. Meanwhile, the wave modes on the corresponding curves also vary with amplitude, typically from local resonances to Bragg scattering, thus impacting on the underlying mechanisms governing the formation of the bandgaps. A dimension reduction of the metamaterials metacell is observed, which occurs due to the degeneration. Moreover, self-adaptive band structures are confirmed by 2DFFT (see Appendix).

The degeneration process depends on the arrangement of the nonlinear components. When nonlinearity exists only between two local resonators as shown in Fig. 12a, the degeneration mainly features bifurcation,

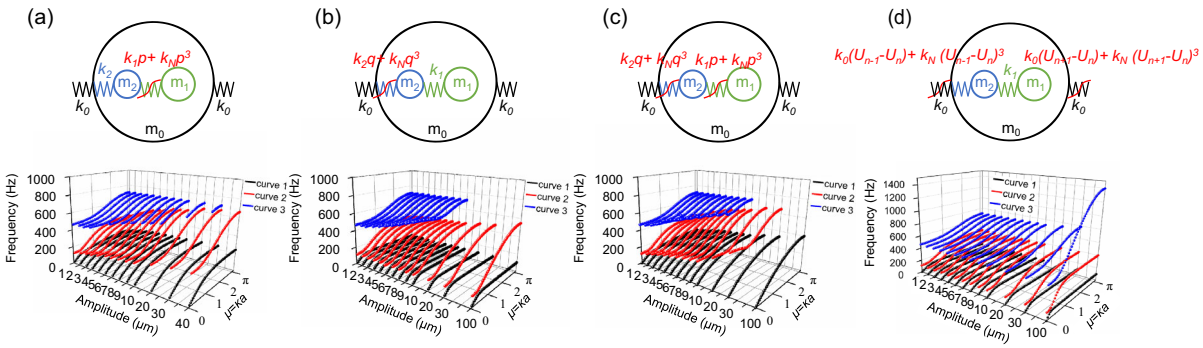

Fig. 12 The comparison of four investigated models in the band structures

shortening and disappearance of high-frequency dispersion curves. Two locally resonant bandgaps merge into a broader resonant bandgap.

When nonlinearity is imposed only between a locally resonator and the primary oscillator as shown in Fig. 12b, the degeneration mainly features the shifting and response disappearance of bands. A locally resonant bandgap evolves into a Bragg bandgap alongside the narrowing-down of the remaining locally resonant bandgap. When both aforementioned nonlinearities are present as shown in Fig. 12c, the two types of behaviors occur simultaneously: i.e., the merging of multiple bandgaps first and then the shifting and band disappearance.

With nonlinearity present in the primary chain as shown in Fig. 12d, there is no band degeneration, but the group velocity of wave undergoes changes. Thus, band degeneration occurs when nonlinearity exists inside at least one local resonator.

6 Conclusion

This paper studies the band degeneration and evolution in strongly nonlinear triatomic metamaterials using analytical and numerical methods. The dispersion curves are solved with harmonic balance method and 2DFFT, which offer consistent results in the near field close to the excitation. Four typical metamaterials models (the triatomic model containing two local resonators) are considered to elucidate the influences of the nonlinear coupling on the band degeneration and evolution.

This work sheds light on the formation and evolution process of the band structure in strongly nonlinear metamaterials and clarifies the underlying mechanisms. This is a generic yet fundamental question to be answered for studying nonlinear periodic structures, nonlinear crystals and nonlinear metamaterials. The results are therefore of interest to the broad community of nonlinear physics.

Acknowledgements This research was funded by the Research Grant Council of the Hong Kong SAR (PolyU 152023/20E). Xin Fang is supported by the National Natural Science Foundation of China (Projects No. 12002371).

Author contributions All authors contributed to the study conception and design. Material preparation, data collection was performed by CG, and analysis was performed by CG, XF and LC. The first draft of the manuscript was written by CG, and all authors commented on the manuscript. All authors read and approved the final manuscript.

Funding The authors have not disclosed any funding.

Data availability The majority data has been shown in this paper. All data for this study, if not included in this published article, are available from the corresponding author on reasonable request.

Declarations

Conflict of interest The authors declare that they have no conflict of interest.

Appendix

Appendix: Adaptive broadening bandgap effects

We take note that the band structures observed and reported in the main text do not consider the influence of the propagation distance, and the numerical dispersion curves are calculated for the first 50 metacells. Fang et al. [39] discovered and experimentally demonstrated that the band structure may adaptively vary with the propagation distance/time, i.e., self-adaptive band structure. In the present case, self-adaptive properties are shown in Fig. 13 through examining the band structures at different positions/segments. Fig. 13a shows the band structure of the first 50 cells as a strong nonlinear case as demonstrated in

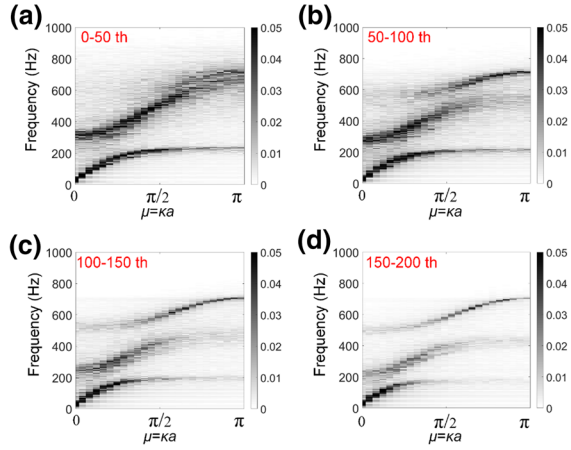

Fig. 13 Band structure of the metacells at different positions/segments with $A_0 = 10$ μm. **a** Metacells from 0 to 50th; **b** Metacells from 50 to 100th; **c** Metacells from 100 to 150th; **d** Metacells from 150 to 200th

Sect. 4.1. When the propagation distance/time increases as shown in Fig. 13b, the band structure of the chain segment containing 50–100th cell exhibits moderate nonlinearity. This is due to the reduced wave amplitude as a result of the wave attenuation in the proceeding cells; meanwhile the broader range will be swept by the new bandgap, leading to increased energy reflection. Given sufficiently large propagation distance/distance increase, the band structure starts to degenerate to a weak nonlinear case, with a band structure similar to that of the linear triatomic chain shown in Fig. 1b. Therefore, the band structure indeed varies self-adaptively as the propagation distance/time increases. In other words, the band structure of a strongly nonlinear metamaterials model varies when the wave energy changes. In addition, this self-adaptive property confirms that the Bloch theorem is no longer applicable to strongly nonlinear metamaterials models, which require the consideration of spatial and temporal variation.

References

1. Fang, L., Darabi, A., Mojahed, A., Vakakis, A.F., Leamy, M.J.: Broadband non-reciprocity with robust signal integrity in a triangle-shaped nonlinear 1D metamaterial. Nonlinear Dyn. **100**(1), 1–13 (2020)
2. Killi, M., Wu, S., Paramekanti, A.: Band structures of bilayer graphene superlattices. Phys. Rev. Lett. **107**(8), 086801 (2011)
3. Esquivel, R., Cocoletzi, G.: Band structure for the propagation of elastic waves in superlattices. J. Acoust. Soc. Am. **95**(1), 86–90 (1994)
4. Banerjee, S., Pal, B.P., Chowdhury, D.R.: Resonance phenomena in electromagnetic metamaterials for the terahertz domain: a review. J. Electromagn. Waves Appl. **34**(10), 1314–1337 (2020)
5. Cummer, S.A., Christensen, J., Alù, A.: Controlling sound with acoustic metamaterials. Nat. Rev. Mater. **1**(3), 1–13 (2016)
6. Chen, S., Fan, Y., Fu, Q., Wu, H., Jin, Y., Zheng, J., Zhang, F.: A review of tunable acoustic metamaterials. Appl. Sci. **8**(9), 1480 (2018)
7. Liu, J., Guo, H., Wang, T.: A review of acoustic metamaterials and phononic crystals. Curr. Comput.-Aided Drug Des. **10**(4), 305 (2020)
8. Fan, K., Padilla, W.J.: Dynamic electromagnetic metamaterials. Mater. Today. **18**(1), 39–50 (2015)
9. Wu, L., Wang, Y., Chuang, K., Wu, F., Wang, Q., Lin, W., Jiang, H.: A brief review of dynamic mechanical metamaterials for mechanical energy manipulation. Mater. Today. **44**, 168–193 (2021)
10. Fang, X., Wen, J., Cheng, L., Yu, D., Zhang, H., Gumbsch, P.: Programmable gear-based mechanical metamaterials. Nat. Mater. **21**, 869–876 (2022)
11. Rothos, V., Vakakis, A.: Dynamic interactions of traveling waves propagating in a linear chain with an local essentially nonlinear attachment. Wave Motion **46**(3), 174–188 (2009)
12. Fiore, S., Finocchio, G., Zivieri, R., Chiappini, M., Garesci, F.: Wave amplitude decay driven by anharmonic potential in nonlinear mass-in-mass systems. Appl. Phys. Lett. **117**(12), 124101 (2020)
13. Rose, A., Smith, D.R.: Overcoming phase mismatch in nonlinear metamaterials. Opt. Mater. Express. **1**(7), 1232–1243 (2011)
14. Rose, A., Smith, D.R.: Broadly tunable quasi-phase-matching in nonlinear metamaterials. Phys. Rev. A. **84**(1), 013823 (2011)
15. Fang, X., Sheng, P., Wen, J., Chen, W., Cheng, L.: A nonlinear metamaterial plate for suppressing vibration and sound radiation. Int. J. Mech. Sci. **228**, 107473 (2022)
16. Cabaret, J., Béquin, P., Theocharis, G., Andreev, V., Gusev, V., Tournat, V.: Nonlinear hysteretic torsional waves. Phys. Rev. Lett. **115**(5), 054301 (2015)
17. Lydon, J., Theocharis, G., Daraio, C.: Nonlinear resonances and energy transfer in finite granular chains. Phys. Rev. E. **91**(2), 023208 (2015)
18. Bonanomi, L., Theocharis, G., Daraio, C.: Wave propagation in granular chains with local resonances. Phys. Rev. E. **91**(3), 033208 (2015)
19. Manktelow, K.L., Leamy, M.J., Ruzzene, M.: Weakly nonlinear wave interactions in multi-degree of freedom periodic structures. Wave Motion **51**(6), 886–904 (2014)
20. Narisetti, R.K., Ruzzene, M., Leamy, M.J.: Study of wave propagation in strongly nonlinear periodic lattices using a harmonic balance approach. Wave Motion **49**(2), 394–410 (2012)
21. Zhou, J., Dou, L., Wang, K., Xu, D., Ouyang, H.: A nonlinear resonator with inertial amplification for very low-frequency flexural wave attenuations in beams. Nonlinear Dyn. **96**(1), 647–665 (2019)
22. Fang, X., Wen, J., Yin, J., Yu, D., Xiao, Y.: Broadband and tunable one-dimensional strongly nonlinear acoustic metamaterials: theoretical study. Phys. Rev. E. **94**(5), 052206 (2016)
23. Fang, X., Wen, J., Yu, D., Yin, J.: Bridging-coupling band gaps in nonlinear acoustic metamaterials. Phys. Rev. Appl. **10**(5), 054049 (2018)
24. Mojahed, A., Gendelman, O.V., Vakakis, A.F.: Breather arrest, localization, and acoustic non-reciprocity in dissipative nonlinear lattices. J. Acoust. Soc. Am. **146**(1), 826–842 (2019)
25. Kanj, A., Wang, C., Mojahed, A., Vakakis, A., Tawfick, S.: Wave redirection, localization, and non-reciprocity in a dissipative nonlinear lattice by macroscopic Landau-Zener tunneling: experimental results. AIP Adv. **11**(6), 065328 (2021)
26. Wang, C., Kanj, A., Mojahed, A., Tawfick, S., Vakakis, A.: Wave redirection, localization, and non-reciprocity in a dissipative nonlinear lattice by macroscopic Landau-Zener tunneling: theoretical results. J. Appl. Phys. **129**(9), 095105 (2021)

27. Wang, S., Nesterenko, V.: Attenuation of short strongly nonlinear stress pulses in dissipative granular chains. Phys. Rev. E. **91**(6), 062211 (2015)
28. Kim, E., Li, F., Chong, C., Theocharis, G., Yang, J., Kevrekidis, P.G.: Highly nonlinear wave propagation in elastic woodpile periodic structures. Phys. Rev. Lett. **114**(11), 118002 (2015)
29. Zhu, H.P., Chen, H.Y.: Parameter modulation of periodic waves and solitons in metamaterials with higher-order dispersive and nonlinear effects. Nonlinear Dyn. **104**(2), 1545–1554 (2021)
30. Fang, X., Wen, J., Bonello, B., Yin, J., Yu, D.: Ultra-low and ultra-broad-band nonlinear acoustic metamaterials. Nat. Commun. **8**(1), 1–11 (2017)
31. Daraio, C., Nesterenko, V., Herbold, E., Jin, S.: Tunability of solitary wave properties in one-dimensional strongly nonlinear phononic crystals. Phys. Rev. E. **73**(2), 026610 (2006)
32. Cabaret, J., Tournat, V., Béquin, P.: Amplitude-dependent phononic processes in a diatomic granular chain in the weakly nonlinear regime. Phys. Rev. E. **86**(4), 041305 (2012)
33. Manimala, J.M., Sun, C.: Numerical investigation of amplitude-dependent dynamic response in acoustic metamaterials with nonlinear oscillators. J. Acoust. Soc. Am. **139**(6), 3365–3372 (2016)
34. Xia, Y., Ruzzene, M., Erturk, A.: Bistable attachments for wideband nonlinear vibration attenuation in a metamaterial beam. Nonlinear Dyn. **102**(3), 1285–1296 (2020)
35. Narisetti, R.K., Leamy, M.J., Ruzzene, M.: A perturbation approach for predicting wave propagation in one-dimensional nonlinear periodic structures. J. Sound Vib. **132**(3), 889 (2010)
36. Bukhari, M., Barry, O.: Spectro-spatial analyses of a nonlinear metamaterial with multiple nonlinear local resonators. Nonlinear Dyn. **99**(2), 1539–1560 (2020)
37. Zhao, C., Zhang, K., Zhao, P., Deng, Z.: Elastic wave propagation in nonlinear two-dimensional acoustic metamaterials. Nonlinear Dyn. **108**, 743–763 (2022)
38. Fang, X., Wen, J., Yin, J., Yu, D.: Wave propagation in nonlinear metamaterial multi-atomic chains based on homotopy method. AIP Adv. **6**(12), 121706 (2016)
39. Fang, X., Wen, J., Benisty, H., Yu, D.: Ultrabroad acoustical limiting in nonlinear metamaterials due to adaptive-broadening band-gap effect. Phys. Rev. B. **101**(10), 104304 (2020)
40. Khajehtourian, R., Hussein, M.I.: Dispersion characteristics of a nonlinear elastic metamaterial. AIP Adv. **4**(12), 124308 (2014)
41. Bae, M.H., Oh, J.H.: Amplitude-induced bandgap: new type of bandgap for nonlinear elastic metamaterials. J Mech Phys Solids. **139**, 103930 (2020)
42. Xia, Y., Ruzzene, M., Erturk, A.: Dramatic bandwidth enhancement in nonlinear metastructures via bistable attachments. Appl. Phys. Lett. **114**(9), 093501 (2019)
43. Wu, Z., Zheng, Y., Wang, K.: Metastable modular metastructures for on-demand reconfiguration of band structures and nonreciprocal wave propagation. Phys. Rev. E. **97**(2), 022209 (2018)
44. Gao, M., Wu, Z., Wen, Z.: Effective negative mass nonlinear acoustic metamaterial with pure cubic oscillator. Adv. Civ. Eng. **2018**, 3081783 (2018)